Latitudinal Dependence of the Kelvin-Helmholtz Instability and Beta Dependence of Vortex-Induced High-Guide Field Magnetic Reconnection

Y. Vernisse, B. Lavraud, M. Faganello, S. Fadanelli, M. Sisti, F. Califano, S. Eriksson, D. Gershman, J. Dorelli, C. Pollock, et al.

Latitudinal dependence of the Kelvin-Helmholtz instability and beta dependence of vortex-induced high-guide field magnetic reconnection

Y. Vernisse[1], B. Lavraud[1], M. Faganello[2], S. Fadanelli[1,3], M. Sisti[2,3], F. Califano[3], S. Eriksson[4], D. J. Gershman[5,6], J. Dorelli[5], C. Pollock[5], B. Giles[5], L. Avanov[5,6], J. Burch[7], J. Dargent[3], R. E. Ergun[4], C. J. Farrugia[8], V. Génot[1], H. Hasegawa[9], C. Jacquey[1], I. Kacem[1], R. Kieokaew[1], M. Kuznetsova[5], T. Moore[5], T. Nakamura[10], W. Paterson[5], E. Penou[1], T. D. Phan[11], C. T. Russell[12], Y. Saito[9], J.-A. Sauvaud[1], and S. Toledo-Redondo[1]

1 Institut de Recherche en Astrophysique et Planétologie, CNRS, UPS, CNES, Université Paul Sabatier, Toulouse, France
2 Laboratoire de Physique des Interactions Ioniques et Moléculaires, Université Aix-Marseille, Marseille, France
3 Physics department, University of Pisa, Pisa, Italy
4 University of Colorado / Laboratory for Atmospheric & Space Physics, Boulder, CO
5 NASA Goddard Space Flight Center, Greenbelt, MD
6 University of Maryland, College Park, MD
7 Southwest Research Institute, San Antonio, TX
8 University of New Hampshire, Durham, NH
9 Institute of Space and Astronautical Science, JAXA, Sagamihara, Japan
10 Space Research Institute, Austrian Academy of Sciences, Graz, Austria
11 Space Sciences Laboratory, Berkeley, CA
12 University of California, Los Angeles, CA

Abstract

We investigate both large- and small-scale properties of a Kelvin-Helmholtz (KH) event at the dusk flank magnetopause using Magnetospheric Multiscale (MMS) observations on 8 September 2015. We first use two types of 3D simulations (global and local) to demonstrate that MMS is close to the most KH unstable region, and so the occurrence of vortex-induced reconnection may be expected. Because they produce low-shear current sheets, KH vortices constitute a perfect laboratory to investigate magnetic reconnection with large guide field and low asymmetry. Recent works suggest that magnetic reconnection may be suppressed when a current sheet combines large guide field and pressure gradient (which induces a diamagnetic drift). We thus perform a statistical analysis of high-resolution data for the 69 KH-induced low-shear magnetic reconnection events observed on that day. We find that the suppression mechanism is not at work for most of the observed reconnecting current sheets, as predicted, but we also find that almost all non-reconnecting current sheets should be reconnecting according to this model. This confirms the fact that the model provides a necessary but not sufficient condition for reconnection to occur. Finally, based on the same dataset, we study the latitudinal distribution of these magnetic reconnection events combined with global magnetospheric modelling. We find that reconnection associated with KH vortices occurs over a significant range of latitudes at the flank magnetopause. It is not confined to the plane where the growth rate is maximum, in agreement with recent 3D simulations.

Keywords

Earth's magnetosphere, space physics, Kelvin-Helmholtz instability, magnetic reconnection

Keypoints

- We use two types of global simulations to locate the KH unstable region at the magnetopause and determine its dynamics.
- We test the diamagnetic-drift reconnection suppression condition over 69 very-low shear current sheets and find an overall agreement.
- We report the broad latitudinal extent of magnetic reconnection locations triggered by KH vortices, consistent with bi-fluid 3D simulations.

1 Introduction

1.1 Kelvin-Helmholtz instability and magnetic reconnection

The Kelvin-Helmholtz instability, which develops in the presence of a sufficient velocity shear between two fluids, has been studied in space plasma physics for several decades [*Chandrasekhar*, 1961; Miura & Pritchett, 1982]. It has been extensively investigated using both observations [e.g. Fairfield et al., 2000; Nykyri et al., 2006; *Foullon et al*., 2010] and numerical simulations in different plasma regimes adopting fluid or kinetic approaches [e.g. *Miura*, 1995; *Wilber and Winglee*, 1995; *Otto and Fairfield*, 2000; *Nakamura and Fujimoto*, 2005; *McNally et al*., 2012]. The recent review paper by *Faganello and Califano* [*2017*] outlines past and recent works on the KHI. Recent advances have shown the importance of KH occurrence at the Earth's magnetopause [*Kavosi and Reader, 2015*; *Lin et al., 2014*] and many works have advocated for its role in plasma transfer at the magnetopause [e.g. *Nykyri et al*., 2017*; Ma et al*., 2017]. Through magnetic field entanglement and torsion, the KH instability provides favorable conditions for the triggering of magnetic reconnection. In particular, evidences for magnetic reconnection induced by a KH instability have been shown to occur within the vortices [*Hasegawa et al*., 2009; *Eriksson et al*., 2016; *Li et al*., 2016] as well as away from the vortices [*Takagi et al*., 2006]. Reconnection is notably triggered at the northern and southern edges of the vortices, caused by the propagation of the magnetic field line entanglement [*Faganello et al.*, 2012a; 2012b; *Borgogno et al.*, 2015; *Vernisse et al*., 2016].

Three types, or rather locations, for magnetic reconnection to occur have been identified in relation with KH waves and vortices. Type I magnetic reconnection [*Liu and Hu*, 1988; *Chen et al*., 1997; *Knoll and Chacon*, 2002; *Nakamura et al., 2008*] is defined as occurring at the compressed current sheet on the sunward face of the KH wave (or trailing edge). Type II reconnection takes place at the leading edge, in the developed vortices of the instability [*Frank et al*., 1996; *Otto and Fairfield*, 2000; *Faganello et al*., 2008; *Nakamura et al.,* 2008], thanks to the interweaving of the magnetic field lines in the more turbulent plasma in this portion of the vortex [*Stawarz et al.,* 2016]. The third type of reconnection is the mid-latitude reconnection scenario, as mentioned above to occur at the northern and southern edges of the vortices. It implies a reconnection process more distant from the equatorial waves or vortices, triggered by the propagation of the magnetic field line torsion in the vortices [*Faganello et al.,* 2012*;*

Borgogno et al., 2015]. This scenario has been studied with data from THEMIS [*Faganello et al.,* 2014] and MMS [*Vernisse et al., 2016*]. In any case, the KH instability either enhances the pre-existing magnetopause current sheet or creates new current sheets because of its own dynamics, finally leading to the development of very low shear magnetic reconnection events whose signatures may be detected by MMS.

Magnetic reconnection is a ubiquitous process that transforms magnetic energy into thermal and kinetic energies. It has been extensively studied in the literature [e.g., *Hesse et al*., 2016; and references therein]. For magnetic reconnection to occur, the change in plasma beta and magnetic shear angle across a current sheet plays a crucial role; it produces a diamagnetic gradient drift that may constitute a suppression mechanism for reconnection [*Swisdak et al.,* 2003*;* 2010]. The vast amount of data gathered throughout the solar system has already largely constrained plasma parameter space for studying this suppression condition for magnetic reconnection. This condition has been tested with success in the solar wind [*Phan et al.,* 2010*; Gosling & Phan,* 2013], the magnetosheath [*Phan et al.,* 2011], the Earth's magnetopause [*Phan et al.,* 2013*; Fuselier et al.,* 2017] and Saturn's magnetopause [*Masters et al.,* 2012]. However, for low beta plasmas ($\beta < 0.1$), the drift-wave instability becomes prominent, and the diamagnetic suppression may be inefficient, as proposed by *Kobayashi et al.* [2014]. More recently, *Liu and Hesse* [2016] investigated diamagnetic suppression in the strong drift limit ($\Delta\beta >> 1$) using a moderate magnetic shear (~90°). By separating the effect of the temperature and density in the pressure gradient term, they concluded that an anisotropy in the temperature allows the slippage of the electron motion relative to the magnetic flux, permitting magnetic reconnection to be maintained.

Owing to the properties mentioned above, KH waves can be used as a dedicated laboratory to study this suppression mechanism in the high guide field limit, which has only occasionally been investigated so far. We perform here a study of high-resolution data from the MMS mission [*Burch et al,* 2015*;* 2016] dedicated to the study of magnetic reconnection at the electron scale. Comparing a set of observed current sheets in between KH vortices, we find that the *Swisdak et al.* [2010] criterion properly predicts reconnecting current sheets, but not the non-reconnecting ones, suggesting this model provides a necessary but not sufficient condition for the triggering of magnetic reconnection.

The paper is organized as follows. In section 2 we analyze the KH events observed by MMS on 8 September 2015 by means of the 3D global MHD simulation code BATS'R'US, provided by NASA's CCMC run on request system (https://ccmc.gsfc.nasa.gov). We then highlight the motion of the KH unstable plane relative to the IMF, as observed in earlier studies [*Farrugia et al.,* 1998]. In section 3, we investigate the properties of magnetic reconnection inside the KH waves, and in particular the conditions for the suppression of reconnection by diamagnetic drift as theorized by *Swisdak et al.* [2003]. In section 4, we combine the 3D MHD simulation and MMS data analysis to conclude on the latitudinal property of magnetic reconnection induced by the KH instability. Conclusions are given in section 5.

1.2 Diamagnetic suppression of magnetic reconnection

Swisdak et al. [2003] proposed that if the diamagnetic drift at a current sheet is faster than the Alfvén velocity associated with the reconnecting magnetic field component, then magnetic reconnection should be suppressed. In order to get such an expression, *Swisdak et al.* [2003] consider a 2.5D equilibrium where all fields are functions of two coordinates, perpendicular to the guide field. First, let us consider that the proper frame (LMN) is a well-determined, right-handed coordinate system, such that M corresponds to the guide field component, N is the component normal to the current sheet, and L is in

the direction of the reconnection outflow. Then, *Swisdak et al.* [2003] show that, at the null line, the ion and electron diamagnetic drift velocities are given by:

$$v_j^* = -q_j c \frac{\nabla P_j \times B}{en|B|^2}\Big|_{null\ line} = -q_j c \frac{\partial_N P_j}{enB_M}\Big|_{null\ line} \cong -q_j c \frac{\Delta P_j}{enL_{CS}B_M}\Big|_{null\ line},$$

where c and e are the speed of light and the Coulomb charge. The terms q and n stand for the charge and density, and B is the magnetic field. The subscript j stands for ion or electron. The term ΔP_j represents the thermal pressure jump across the current sheet. L_{CS} is the half-width of the current sheet. In principle, if we assume the homogeneity of the thermal pressure and of the plasma properties in general (i.e., the medium surrounding the x-point varies infinitesimally), the ansatz is valid. Let us focus on the pressure variation term. Using the pressure tensor expressed in the LMN frame, the N component of the pressure divergence reads:

$$\partial_N P = \partial_L P_{LN} + \partial_N P_{NN} + \partial_M P_{NM}$$

Assuming that the off-diagonal terms are negligible, the diamagnetic drift for each species becomes

$$v_j^* \cong -q_j c \frac{P_{j,NN}^{sh} - P_{j,NN}^{sp}}{enL_{CS}B_{M,null\ line}},$$

where the super-scripts “sh” and “sp” stand for magnetosheath and magnetosphere, respectively. To express the suppression condition, we have to explicit the ion Alfvén velocity in the direction of the exhaust (L):

$$v_{A,L} = \frac{B_{L,asymptotic}}{\sqrt{4\pi m_i n_{i,null\ line}}}$$

Thus, the diamagnetic suppression criteria

$$|v_i^*| + |v_e^*| > v_{A,L}$$

leads to

$$P_{j,NN}^{sh} - P_{j,NN}^{sp} > \frac{2L_{CS}}{d_{i,null\ line}} \frac{B_{M,null\ line} B_{L,asymptotic}}{8\pi} \quad (1)$$

where $d_{i,null\ line}$ is the ion inertial length at the null line. Another way of expressing this condition uses the plasma β on both side of the current sheet versus the magnetic shear angle θ. In order to get such an expression, from:

$$\frac{P_{j,NN}^{sh} - P_{j,NN}^{sp}}{{B_{M,null}}^2/8\pi} = \frac{2L_{CS}}{d_{i,null\ line}} \frac{B_{L,asymptotic}}{B_{M,null\ line}},$$

we finally get:

$$\Delta\beta_M > \frac{2L_{CS}}{d_{i,null\ line}} \tan\frac{\Theta}{2} \quad (2)$$

However, to obtain the last expression one needs to assume that the guide field is constant across the current sheet. This last expression should be used carefully, in particular because the plasma β must be

derived with only the NN component of the pressure tensor, as well as only the M component of the magnetic field for the magnetic pressure. Furthermore, one may argue that such a definition of a plasma β does not possess a proper physical meaning and can hardly be interpreted.

To complete the picture, the expression often used in the literature [e.g. *Gosling and Phan*, 2013; *Masters*, 2014; 2015] is as follows

$$\Delta\beta = \frac{2L_{CS}}{d_i}\tan\frac{\theta}{2} \quad , \tag{3}$$

where $\Delta\beta$ stands for the difference between the total plasma β on the two sides of the current sheet and θ is the shear angle between the magnetic fields on the two sides of the current sheet (with no specific component). This last equation, however, suffers from several simplifications of the suppression model, as it does not take into account the exact quantities at stake here.

In the following section, we briefly investigate the validity of each formulation, and in particular the validity of equation (3) with respect to the exact expression in equation (1).

2 Numerical simulations of the event

2.1 Global MHD simulation

In order to locate properly the Kelvin-Helmholtz instability at the magnetopause, and to compare with observations, we requested runs of global MHD simulation codes from NASA's Community Coordinated Modeling Center (CCMC) for the global magnetospheric models BATS'R'US [*Powell et al.,* 1999] and OpenGGCM [*Raeder et al.,* 2008]. The simulations were initialized with OMNI data [*King and Papitashvili,* 2005], using the time interval during which the Kelvin-Helmholtz instability was observed by the MMS satellites, on 8 September 2015 between 9:30 and 11:30 UT. We also ran simulations using THEMIS B data, which was located in the solar wind during the whole event. The results are similar to those using the OMNI data as shown here. MHD simulations use exclusively a constant IMF B_x at the solar wind input. The results presented here thus do not properly account for the IMF cone angle. To mitigate this limitation, we utilize a local 3D bi-fluid simulation in the next section to confirm the locations of KH growth and reconnection.

Results of the simulation runs from BATS'R'US are presented in Figure 1. Results from OpenGGCM are essentially similar and are not shown here. Figure 1a provides a three-dimensional representation of the growth rate on the magnetopause surface, as derived from the output of the BATS'R'US simulation run. We detect the magnetopause from the simulation data using the methodology detailed in Appendix A. We compute the Kelvin-Helmholtz instability growth rate at the detected magnetopause using the formula from *Chandrasekhar* [1961] for a discontinuous shear layer:

$$\left(\frac{\gamma}{k}\right)^2 = \frac{\rho_{sh}\rho_{sp}}{(\rho_{sh}+\rho_{sp})^2}\left(\left(\boldsymbol{\Delta U}\cdot\widehat{\boldsymbol{k}}\right)^2 - \frac{1}{\mu_0}\left(\frac{1}{\rho_{sh}}+\frac{1}{\rho_{sp}}\right)\left(\left(\boldsymbol{B_{sh}}\cdot\widehat{\boldsymbol{k}}\right)^2 + \left(\boldsymbol{B_{sp}}\cdot\widehat{\boldsymbol{k}}\right)^2\right)\right) \tag{4}$$

where the term ΔU is the differential velocity between the magnetosphere and the magnetosheath. The terms ρ and B are the density and magnetic field, while the indices ('sh' and 'sp') stand for magnetosheath and magnetosphere, taken at one Earth radius on each side of the identified magnetopause. The distance to the magnetopause chosen to derive the growth rate is arbitrary, taking

into account the limited resolution of the simulation. We do not investigate the plasma penetration in the magnetosheath that appears in global MHD simulations [*Li et al.*, 2009].

We use the velocity and magnetic field projected in the plane tangent to the magnetopause for each point. We search for $\widehat{\boldsymbol{k}}$ (normalized wave vector) such that it maximizes the above equation. The results are represented on a surface derived from the magnetopause model by *Shue et al.* [1997] (cf. Appendix A). Negative solutions of the growth rate are ignored and set to zero in Figure 1. The global amplitude of the growth rate is consistent with the amplitude derived from the MMS data, which give $\frac{\gamma}{k} = 135\ km/s$ [*Eriksson et al.,* 2016]. It is worth noticing that the *Chandrasekhar* [1961] relation (4) neglects any effect due to the finite thickness of the velocity shear layer that reduces the growth rate and stabilizes short wavelengths [see *Faganello and Califano*, 2017, for further details]. This formula represents a first indication for the magnitude of the growth rate and shows the role of the velocity jump (projected on the wave vector direction) in driving the instability and the stabilizing role of the magnetic tension due to field line distortion when the magnetic field has a component along the flow shear.

In Figure 1a, the whole orbit of the MMS spacecraft on 8 September 2015 is plotted in blue, in the GSM coordinate system. We show the equator and the terminator with black lines. The Earth is at the center of the plot. A magnetic field line, derived from the simulation data, connected to the southern hemisphere on one side and connected to the solar wind on the other side is also displayed in red. We will refer to this magnetic field line in the following sections for context. Figures 1b and 1c (1d and 1e) show the growth rate (magnetic field shear) at the identified magnetopause at two simulated times, 9:50:00 UT and 11:14:00 UT, respectively. The orientation of the IMF in the (Y_GSM, Z_GSM) plane is represented with a white arrow in the plots and the position of the MMS spacecraft (from 9:30 UT to 11:30 UT) is represented by black dots in Figures 1b and 1c, and by white dots in Figures 1d and 1e.

In Figure 1a, the three dimensional distribution of the growth rate at the magnetopause highlights the large-scale configuration of the KH unstable region at the magnetopause. In Figure 1b, we observe that although the IMF clock angle is low (10°), the dusk part of the KH unstable region is slightly shifted to the southern hemisphere, while the dawn side of the unstable region is shifted towards the northern hemisphere. In accord with *Farrugia et al.* [1998], this trend is more pronounced in Figure 1c for a clock angle of 30°. On the dusk side of the magnetopause, the most unstable region is shifted towards negative latitudes. This shift of the KH unstable region is consistent with the distribution of magnetic shear angle shown in Figure 1d and 1e. In Figure 1e, the MMS spacecraft were clearly cruising in the minimum magnetic shear angle region. These results highlight that the MMS spacecraft were well located to observe KH waves during the event, for these particular solar wind and IMF conditions.

2.2 Local 3D two-fluid simulation

We now analyze a local 3D two-fluid (Hall-MHD) simulation of the dusk flank to further demonstrate the KH development and vortex rolling-up during this event, confirming the fact that MMS satellites are well located and consistent with the occurrence of induced reconnection. This simulation starts from a modeled equilibrium, as in *Fadanelli* et al. [2018] that takes as asymptotic values (far away from the magnetopause) the plasma quantities measured during the event [*Eriksson et al.*, 2016] in the boundary layer (outer magnetosphere) and in the magnetosheath plasma depletion layer (e.g., *Wang et al.*, 2004), respectively. A three-dimensional rendering of the simulation is given in Figure 2b. In this simulation the linear KH growth rate, associated to the equilibrium, gradually decreases as $|z|$ increases from $|z| = 0$,

where z is the (signed) distance from the z= 0 (coined equatorial plane hereafter), expressed in KH wavelength units ($\lambda_{KH} \approx 12000\ km$ as given by the observed average period $\approx 60s$ of KH oscillations and a phase-velocity $\approx 200\ km/s\ \geq 1/2\ \Delta U$, with $\Delta U \approx 350 km/s$ being the observed velocity jump). This is observed in Figure 2a, where the growth rate drops at the box outer boundaries (located at $z = \pm 4\lambda_{KH} \approx \pm 48000\ km$) to a third of its value at $z = 0$.

In Figure 2b, we show the simulation results at the beginning of the non-linear phase. KH vortices develop in a wide latitude range across the equatorial plane (z = 0). Well-formed rolled-up structures are present from $z = -\lambda_{KH} \approx -12000\ km$ to $z = +3\lambda_{KH} \approx 36000\ km$, as shown by the folded magnetopause, while the magnetopause at $z = \pm 4\lambda_{KH} \approx \pm 48000\ km$ is nearly unperturbed. The KH development is asymmetric with respect to the equatorial plane, as expected when a flow-aligned component of the IMF is present [*Fadanelli et al*., 2018], even if all the other fields are symmetric. In the present case with $B_{IMF} \cdot U_{SW} < 0$ the vortices develop more vigorously for z > 0, as expected. Although weaker for z < 0, they are still well formed at $z = -\lambda_{KH} \approx -12000\ km$ where the MMS satellites are predicted to be if we refer to Figure 1b. More quantitatively, we estimate the value of the angle between the unperturbed magnetopause normal (the X axis in the simulation) and the actual normal measured in the simulations at the trailing (sunward facing) edge of the KH waves. This angle, which we term "trailing angle", is shown in Figure 2c as a function of z at the beginning of the non-linear phase. The maximum value is around 35° and is located, as expected, in the upper part of the simulation domain where the vortices are most developed. In the bottom region, its value is smaller but at $z = -\lambda_{KH} \approx -12000\ km$ it is still compatible with the values measured by MMS (as we will discuss in Section 4). Moreover, the folding time of the vortices in our simulation $\tau_{fold} = \gamma_{KH,3D\ sim}^{-1} \approx 92s$, in dimensional units, is compatible with the time KH waves take to travel (at a phase-velocity $\approx 200\ km/s$) from a longitude of 30° to the MMS longitude. This fact suggests that KH vortices have time to fully develop before reaching the satellites.

Green regions in Figure 2b show where the magnetic field develops a component perpendicular to the local magnetopause as observed in the simualtion in the non-linear phase. This normal magnetic field component, as defined and studied already in *Faganello et al.* [2012], would not develop in an ideal MHD evolution where the frozen-in condition is satisfied. This normal component was shown in *Faganello et al.* [2012] to be a clear signature that magnetic reconnection is occurring on the magnetopause, thereby the large-scale magnetic topology.

In summary, global simulations of the whole magnetosphere as well as a local simulation of the KH instability on the dusk flank magnetopause, indicate that the MMS satellites are in the proper location to detect well developed KH structures and, as a consequence, magnetic reconnection induced by the vortices. Furthermore, the local simulation suggests that reconnection proceeds on a wide latitude band as already observed in numerical simulations starting from a configuration similar to the present one [*Fadanelli et al*., 2018].

3 MMS data analysis

3.1 Event illustration

On 8 September 2015, between 10:00 and 11:30 UT, the four MMS spacecraft sampled a long duration KH wave interval on the dusk side of the dayside magnetosphere [*Eriksson et al.,* 2016*; Li et al.,* 2016*; Vernisse et al.,* 2016]. We recall the context of the event in Figure 3. The clock angle and the cone angle shown in Figure 3a are from OMNI data [*King and Papitashvili,* 2005]. Figures 3b, 3c, and 3d display the magnetic field, ion bulk velocity, and ion plasma beta measured by the MMS1 spacecraft between 8:00 and 13:00 UT. Although the IMF was mostly northward, the clock angle varied from a minimum of 15° (at 10:45 UT) to a maximum of 40° (at 11:10 UT). In section 3.2, we perform a statistical analysis on 69 magnetopause crossings observed during the event. Our statistics focuses on the trailing edge (also known as sunward edge) of the KH waves. This side of the KH wave has the thinnest current sheet and the distinction between the magnetospheric and magnetosheath plasma is easily made from the data. In order to determine whether the current sheet is reconnecting or not, we first perform a double Walén test (i.e., with positive and negative slopes each side of a possible ion jet; e.g. *Phan et al.,* 2004) on all the current sheets and verify if a reconnection jet is identifiable. We first base our work on the identifications provided by *Eriksson et al.* [2016], and revisit it with the newly available burst data (we provide all data in the supplementary material). Typical Walén tests that have been performed in order to identify potential reconnection jets are illustrated in Figures 3e to Figures 3n. Figures 3e and 3j show the magnetic field in a local LMN coordinate system as described in *Eriksson et al.* [2016] and *Vernisse et al.* [2016], which we recall here. We perform a minimum variance analysis [MVA, *Sonnerup and Scheible,* 1998] on the current sheet to determine the L vector (the largest variance direction). The current sheet normal (N vector) is derived using the cross product of the magnetosheath and magnetosphere magnetic field. The M vector completes the coordinate system and is directed along the northward pointing guide field. Figure 3f and 3k present the L component of the velocity. Figure 3g and 3l show the electron pitch angle distributions, for energies between about ~274 eV and ~577 eV. Figure 3h and 3m show the ion plasma beta, while Figure 3i and 3n show the electron plasma beta.

The first and second black lines in Figure 3e to 3n delimit the main magnetopause current sheets. They are identified based on the decrease in plasma Beta (increase in density and decrease in temperature and magnetic field towards the magnetosheath), the decrease in suprathermal electron phase space density, and the magnetic field By variation (corresponding to a B_L variation), which is the typical main component varying at the trailing edge of KH waves at this location [e.g., *Eriksson et al.* , 2016]. Only the first event, in figures 3e to 3i, show typical signatures of a reconnection jet. This is corroborated by the Walén test in Figure 3f (albeit more qualitatively than quantitatively), where the L component of the velocity is plotted together with the variation of the Alfvén velocity as calculated from the magnetic field and density [*see e.g. Phan et al.,* 2004]. Clearly, in this first case, a jet is observed. In addition to identifying the signature of a jet in the ion bulk velocity, we searched for the possible presence of electron leakage from the magnetosphere to the magnetosheath [e.g., *Fuselier et al*., 1995; 1997; *Onsager et al*., 2001; *Lavraud et al*., 2005; 2006]. Figure 3g shows a typical signature of such a leakage, identified by the increased electron flux in the field-aligned direction between the second and the third black vertical lines, outside the magnetopause in the magnetosheath boundary layer. This confirms that these field lines are open because of reconnection. By contrast, the current sheet delimited by the vertical black lines in Figure 3j to 3n presents no evident signatures of reconnection. There is no obvious jet between the black vertical lines in Figure 3k (there is a change in velocity across the current sheet, but this corresponds to a large-scale change induced by the vortex structure, from inside the MP to outside in the magnetosheath, rather than a jet). Correspondingly, we do not observe any electron leakage in Figure 3l after the current sheet.

3.2 Statistical analysis of current sheets

Here we analyze the 69 current sheets identified during the KH event observed by MMS1 on 8 September 2015 (cf. supplementary material). Our analysis is as follows. We record the start and end times of each current sheet by hand. We define for each crossing a magnetosphere interval and a magnetosheath interval. The magnetosphere interval corresponds to three seconds of data before the start of the current sheet (e.g., three seconds on the left side of the first vertical black line for the case in Figures 3e to 3n). The magnetosheath interval corresponds to three seconds of data after the end of the current sheet (e.g. three seconds on the right side of the second vertical black line in Figure 3e to 3j). We derived the reference magnetosphere and magnetosheath parameters by averaging data on these intervals. In addition, we project both the velocity and magnetic field on the local LMN coordinate system defined above for each current sheet crossing.

We now confront MMS observations with the magnetic reconnection suppression model proposed by *Swisdak et al.* [2003] in Figure 4. In the first, second, and third columns of Figure 4 we confront Equations (1), (2), and (3), respectively, with our data analysis. For the derivation of Equation (1), we evaluate the pressure difference using the NN component of the pressure tensor expressed in the local LMN frame. Similarly, $B_{L,asymptotic}$ (noted $B_L$in Figure 4 for the sake of concision) is the L component of the magnetic field evaluated as follow: $B_{l,asymptotic} = |\frac{\langle B_{L,sheath}\rangle - \langle B_{L,sphere}\rangle}{2}|$, where <…> represents the mean operator (used on data from the magnetosphere and magnetosheath intervals as defined above). The term $B_{M,null}$ (cf. introduction; noted B_M in Figure 4) is the M component of the magnetic field averaged over the current sheet traversal. The evaluation of Equation (2) requires the same quantities as Equation (1). We evaluate Equation (3) using the difference of the total plasma β averaged over the magnetosheath and magnetosphere intervals, respectively. The magnetic shear θ is evaluated as: $\theta = \arccos(b_{L,sheath} * b_{L,sphere} + b_{M,sheath} * b_{M,sphere})$, where $b_L = B_L/|B|$. We derive all error bars by computing the standard deviation of each quantity during the 3-seconds intervals (and propagating it when required).

To confront our observations with the *Swisdak et al.* [2003] model, in a fashion similar to past studies [e.g.*, Phan et al*., 2013], we first need to determine whether the observed current sheets were reconnecting or not. We used three criteria for that purpose. As also explain in the previous section, the first criterion is the presence of a reconnection jet, visually identified by an ion velocity enhancement with consecutive positive and negative correlations with magnetic field changes, i.e., using the Walén test as illustrated in Figure 3 (first case). The second criterion for identifying reconnection is the identification of an electron boundary layer on the magnetosheath side of the current sheet, signaling the leakage of heated electrons along open field lines ensuing from reconnection. The directionality of heated leaking electrons (parallel or anti-parallel to the magnetic field) provides clues on the location of the X line relative to the spacecraft location (along the magnetic field) [e.g., *Fuselier et al.*, 1997; *Onsager et al.*, 2001; *Lavraud et al.*, 2006]. There is a straight link between the directionality of leaking electrons and the direction of the reconnection jet [*Vernisse et al.*, 2016]. Owing to the geometry of the event and the trajectory of the spacecraft, we expect to observe, on the magnetosheath side of the current sheet, electrons leaking parallel to the magnetic field when the jet is directed toward the –L direction (also seen as a decrease in the V_L component). Similarly, electrons leaking anti-parallel to the magnetic field in the magnetosheath are expected when the jet is directed along +L is observed; this corresponds to an

increase in the V_L component. The observation of a reconnection jet together with an electron leakage signature is thus deemed "consistent" if their directions are in the appropriate sense relative to the expected reconnection geometry.

Those identifications are presented in Figure 4. We categorize events following their likelihood of being reconnecting events. The first category shown in Figure 4a to 4c ('jets & ebl consistent') represents crossings where an ion jet and a consistent electron boundary layer are observed. The consistency between those two observations is illustrated in *Vernisse et al*. [2016] (Figure 3) and *Li et al.* [2016] (Figure 1), with the same configuration. The second category ('jets & ebl present but not consistent'), in Figures 4d to 4f, is made of cases where both a jet and an electron layer were identified, but they were not consistent with each other (in terms of the directionality of the jet and the electrons, as explained above). The third category ('only jets'), in Figure 4g to 4i, is based on events that present only a clear reconnection jet, and the fourth category ('only ebl'), in Figure 4j to 4l, is made of cases where only an electron boundary layer was clearly observed. The fifth category ('no jet and no ebl'), in Figure 4m to 4o, gathers crossings where neither a reconnection jet nor an electron boundary layer was observed. We provide a plot with all events in Figure 4p to 4r for sake of completeness. Equations (1), (2), and (3) are plotted in each Figure for three values of current sheet thicknesses, $L_{eq} = 0.5, 1, and\ 2\ d_i$ (where d_i is the ion inertial length), in red, black, and blue, respectively. Points located under the curves should be non-reconnecting events according to the *Swisdak et al.* [2003] criterion. In brief, going down in each row of Figure 4, events are displayed such that they have less and less likelihood to be reconnecting events. In other words, there should be a tendency for all points in Figures 4a to 4c to be located above and/or to the left of the main curve, while points would, in principle, rather be located below and/or to the right of the curve in Figures 4m to 4o.

Several points have to be emphasized from Figure 4. The first thing to notice is the similarity of the results in the first and second column. This suggests that the hypothesis on the steady character of the guide field (see Section 1.1) across the current sheet is justified.

Secondly, the results in the third column (for Equation (3)) are different from the first and second columns. We notice that more points are located under the red curve in Figure 4c than in Figure 4a and 4b. A similar behavior is noticeable in Figure 4l where several points stand under the black curve, while all points are above the black curve in Figures 4j and 4k. This means that Equation (3) tends to overestimate the suppression mechanism. The main difference comes from the derivation of the plasma β, which in Equation (3) requires both the parallel thermal pressure and the B_L component of the magnetic field. For the observed events, the addition of the parallel pressure in the plasma β term plays the main role.

As mentioned by *Swisdak et al.* [2010], the fact that the properties of a current sheet show conditions favorable for reconnection in the framework of this theory is a necessary but not sufficient condition for reconnection to occur. In that context, Equations 1 and 2 (Figure 4a and 4m) are in agreement with this assertion. However, Equation 3 is not, pointing to the need to use the proper component of the pressure tensor and magnetic field across the current sheet, when available. In this latter regard, we note that past studies (cf. introduction) typically did not have access to the full pressure tensor at sufficient resolution.

Thirdly, no clear trend is visible between the 5 classifications of events, and for all three models. As mentioned above one should expect a trend on the position of the points relative to the curve

depending on whether reconnection is ongoing or not. In particular, more and more points should move under the curve as we consider current sheets for which signatures of reconnection are less evident or even totally absent. We further discuss this lack of trend in the next sections.

3.3 Possible limitations

We must mention that our classification of the events may be biased in several ways. As we are studying small-scale current sheets, it is always possible that the reconnection jet or the electron boundary layer may be missed owing to proximity to the X line and/or insufficient time resolution. This is particularly true for the ion jets, which may not be observed if too close to the X line. We identified a few events that seem to possess an electron jet possibly consistent with a crossing close to the X-line. However, we leave the detailed analysis of such electron jets for future work. This limitation, in any case, is very unlikely to affect the electron boundary layer observations given the very high resolution of the MMS data (in particular as compared to past studies on the topic that were using much coarser resolution).

In addition, the compressed current sheet at the trailing edge of KH waves may be populated of numerous flux rope-type magnetic structures, as has been found in recent observations and simulations [*Eriksson et al*., 2009; *Nakamura et al.* [2011; 2013; 2017a; 2017b]. This complexity of the current sheet may perturb the expected signatures both in terms of ion jet and electron boundary layer.

3.4 Implications for existing models of magnetic reconnection suppression

Despite these possible observational limitations, the lack of ordering of the reconnecting and non-reconnecting cases with respect to the theoretical curves (Figures 4a and 4m) suggests that the conditions provided by Equation (1) may not be sufficient in the specific regimes of nearly symmetric, high guide field reconnection such as here when induced by the KH instability. Recent studies have already revealed that the diamagnetic suppression may be mitigated in certain regimes. *Kobayashi et al.* [2014] investigated the diamagnetic suppression by means of gyrokinetic simulations, and found that in the regime of low plasma beta ($\beta < 0.1$), the diamagnetic suppression is mitigated by the drift wave instability (which is prominent in that regime). A study by *Liu and Hesse* [2016] recently examined the regime of moderate magnetic shear (~90°) and high beta difference (~20). In particular, they dissociated the role of the temperature and density gradients, which both account for the pressure gradient responsible of the suppression, and found that while the density gradient provides results similar to the global pressure gradient, the temperature gradient acts differently: a strong pressure gradient generated only by a strong temperature gradient does not suppress reconnection. Thus, disentangling the impact of the density gradient and the temperature gradient shall be performed in future work but falls out of the scope of the present paper. Neither of these studies, however, investigated the particular regime of low magnetic shear angle (< 60°) and moderate beta difference (~1). Further theoretical and observational studies are thus needed to determine whether a dedicated model is required in the high guide field reconnection regime.

We investigate in Figure 5 the possible role of the thickness of each current sheet. We derived the thickness of each current sheet using the mean of the N component of the ion bulk velocity, obtained with the cross-product method detailed earlier, over the current sheet crossing duration. We also used

the differential timing method [*Harvey*, 1998] to get the normal velocity and derive the current sheet thicknesses. Results from both methods are similar, thus we only present results using the cross product here. Figure 5a shows the distribution of the current sheet thickness for each category of event. Figure 5b shows the cumulative distribution for each case to best demark the differences between these distributions. These show that the current sheet thicknesses are rather homogeneous, except for the events showing no clear signature of reconnection (no jet and no ebl). This is best observed in Figure 5b, with a marked difference between the cumulative distribution of non-reconnecting events (red curve) and the others. The average thicknesses of the distributions of the sets of events are $4.8\ d_i, 5.66\ d_i, 4.57\ d_i, 6.24\ d_i$, and $9.29\ d_i$, with standard deviations of $3.16\ d_i, 2.39\ d_i, 1.75\ d_i, 5.76\ d_i$, and $6.98\ d_i$, respectively for each category: "jet and ebl consistent", "jet and ebl present but not consistent", "only jets", "only ebl", and "no jet and no ebl".

This finding is interesting. At first sight, it could suggest that these current sheets are non-reconnecting because of their overall larger thicknesses, a factor that is known to be important for reconnection to trigger [*Priest & Forbes*, 2000]. However, in the context of an asymmetric current sheet a small thickness in fact also implies a stronger gradient drift for the same asymptotic boundary conditions. Although somewhat counterintuitive, this observation in fact rather increases the inadequacy of our results with respect to the *Swisdak* et al. [2003] model. In other words, what this means is that in Figures 4m, 4n, and 4o (for non-reconnecting current sheets) one should compare the distribution of points to the blue curve (or even more to the right, since a large thickness decreases the pressure gradient and ensuing gradient drift suppression effect) rather than to the black or red ones. Thus, in principle, almost all events should be reconnecting, or at least their conditions do not preclude reconnection from occurring.

Importantly, it must then be noted that if an event presents reconnection signatures and can be categorized as "reconnecting", then the thickness would correspond to the thickness of the exhaust and not at all to the thickness of the initial current sheet before reconnection is triggered (while the latter is that relevant to the *Swisdak et al.* [2003] model). By contrast, for non-reconnecting current sheets, the measured thickness does correspond to the thickness that is relevant to the triggering of reconnection in the *Swisdak et al.* [2003] model. Again, in this context, according to Figures 4 and 5, most of the cases should in fact be reconnecting given the fact that for current sheet thicknesses equal or superior to 2 inertial lengths the *Swisdak* et al. [2003] condition for reconnection is satisfied. However, we recall that this condition is necessary but not sufficient, as mentioned in *Swisdak et al.* [2016]. The present findings are thus consistent with the model.

Finally, it may also be noted that the rather thin, and homogeneously distributed, current sheet thicknesses of reconnecting events in Figure 4a, together with the fact that reconnecting current sheets are on average thinner than non-reconnecting ones, suggest that it is unlikely that we miss many thin reconnecting current sheets in our analysis. In other words, the temporal resolution of the MMS data should allow us not to miss a lot of reconnection jet.

4 Latitudinal dependence and three dimensional properties of the KH instability and induced reconnection

As shown in the literature by means of three-dimensional MHD [*Ma et al.*, 2017] and multi-fluid simulations [*Faganello et al.*, 2012; 2014, *Borgogno et al.,* 2015], the limitation of the Kelvin-Helmholtz

instability to a two dimensional setup misses several key aspects of its development and ensuing topological properties. In Figure 6 we study the latitudinal distribution of the KH-induced reconnection events studied in section 3. As introduced in Section 2, we also performed a BATS'R'US simulation of this event, initialized with actual OMNI data. The same simulation using THEMIS B data as inflow conditions (sitting in Earth's upstream solar wind at that moment) showed no significant differences and is thus not presented.

For each data point of the MMS1 spacecraft location, we look for the maximum growth rate position on the same meridian in the global MHD simulation and measure the latitudinal distance of the spacecraft to this maximum growth rate. For that purpose, we use the time of each current sheet crossing from the MMS1 data to find the corresponding simulation output time to use, and to derive the location of the KH unstable region. The result of this analysis is presented in Figure 6a, where all current sheet crossings are categorized using the five types of signatures introduced in section 3.2.

Figure 6a presents each current sheet according to its distance to the maximum growth rate plane in terms of latitude angle plotted as a function of the angle between the normal to the unperturbed magnetopause (derived from the *Shue et al.* [1997] model) and the normal to each current sheet (derived using the cross-product method). We name the latter quantity "normal angle" for conciseness (it is similar to the trailing angle defined for the local simulation in Section 2.2). A range of 20° is covered in terms of spacecraft distance to the simulated maximum growth rate plane. The MMS spacecraft were thus cruising all the time fairly close to the maximum growth rate plane, but yet over a non-negligible range of latitudes and essentially on the southern side of the maximum growth rate plane. We also display in Figure 6a the directionalities of the ion jets with arrows, in accordance with the corresponding magnetic field geometry. Magnetic reconnection jets were observed southward and northward of the spacecraft, independently of their position relative to the most unstable plane, thus suggesting that the possible locations of reconnection triggering cover an extended latitudinal region relative to the maximum growth plane.

We note that events that are likely reconnecting (blue, cyan, and green points) appear somewhat less spread, in both normal angle and separation to the unstable region, than non-reconnecting cases (orange and red points). In terms of latitudinal spread, the computation of the standard deviation for each set of points gives 4°, 5.2°, 5°, 5.6°, and 5.7° from most likely reconnecting (blue) to less likely reconnecting (red) cases. This signals that the area of observation of reconnecting jets is less dispersed in latitude relative to the maximum growth rate plane, with a mean location 10° southward of that plane. Cases where no reconnecting jets are observed are found over a broader latitude range, suggesting no particular correlation with latitude. This property is consistent with a previous study [*Faganello et al.,* 2012] showing that, in KH instabilities, reconnection occurs mostly away from the most unstable plane, due to the propagation of the twisting of the magnetic field.

Figure 6b presents time series of the latitude distance between the spacecraft and the maximum growth rate plane (red line) for each simulation output. Additionally, we show the IMF clock angle from OMNI (blue line) and the "normal angle" (black line). The distribution of this angle between the local current sheet normal and the unperturbed magnetopause shows that the vortices are broadly distributed over a range of latitudes, and seem not to be limited to the most unstable region. This suggests that the spacecraft are observing rather local signatures of reconnection, i.e., induced by the vortices (type I), rather than signatures of mid-latitude reconnection at the southern end of the unstable region.

However, as was recently shown in *Fadanelli et al.* [2018], when a non-negligible magnetic shear exists (non-purely parallel magnetic fields across the flank magnetopause; or in other words non-purely northward IMF), KH-induced reconnection is not limited to specific regions around the vortices (inside, below or above). It is rather triggered over a broad and continuous range of locations near the vortices, so that the distinction between mid-latitude and type I (Vortex-induced) reconnection is harder to make, if at all meaningful, as also suggested in a recent simulation of this event by *Sisti et al.* [2019]).

5 Conclusions

We studied the properties of Kelvin-Helmholtz induced magnetic reconnection by means of 3D MHD and two-fluid simulations and data analysis from the MMS mission. The global simulation demonstrates that the location of the most unstable KH region at the Earth's magnetopause is not confined to the equatorial plane, but rather distributed over a range of latitude, and shifted to the northern or southern hemisphere, depending on the upstream IMF clock angle. The two-fluid simulation particularly confirms this point, as also shown in *Fadanelli et al.* [2018], with a clear shift of the vortices location.

We then investigated magnetic reconnection on a local scale within the KH vortices, and in particular on the trailing edge of the waves. Owing to the typical large-scale configuration at the magnetospheric flanks where the KH instability develops, magnetic reconnection induced by KH waves has a strong guide field component. This is of particular interest to study the onset properties of magnetic reconnection under such conditions. We tested the model proposed by *Swisdak et al.* [2003] and found that all observed events fulfilled the condition for reconnection to occur, including those without reconnection signatures. This shows that the diamagnetic suppression condition works also in that regime, but the fact that all non-reconnecting events are found in "possibly" reconnecting conditions confirms that this model provides a necessary but not sufficient condition for reconnection to occur.

In addition, thanks to the high quality of the MMS data, we were able to derive several variants of the suppression condition for each observed event. The most accurate variant makes use of the full pressure tensor and was not used in previous studies based on different datasets. We show in our study that the use of a simplified model can lead to a significant under-estimation of the range of conditions that are favorable for reconnection.

Finally, by combining simulations and data analysis we found that the reconnecting current sheets observed by MMS are broadly distributed (20°) and all southward of the most unstable region at the magnetopause. This finding is consistent with recent simulations by *Fadanelli et al*. [2018] and *Sisti et al.* [2019] suggesting that magnetic reconnection occurs over a broad range of latitudes, and so that vortex-induced (type I) and mid-latitude reconnection are hard to separate when a significant magnetic shear exists at the flank magnetopause (i.e., non-purely northward IMF).

APPENDIX A: Magnetopause detection procedure in the global MHD simulation code BATS'R'US

In order to derive properly the growth rate at the Earth's magnetopause, we need to find the magnetopause position in the simulation run. Our method is as follows. (1) We initialize a magnetopause surface using the *Shue et al.* [1997] model and the upstream parameters of the simulation. The modeled

distance is systematically larger than that in the global MHD run. For each point at the magnetopause, we search for the maximum current density, using a Gaussian fit, along the normal to the magnetopause as estimated from the *Shue et al.* [1997] model. We illustrate this magnetopause detection scheme in Figure 7, which shows the current density and the X_{GSM} component of the velocity in the meridional plane, the equatorial plane, and on a plane at 45° between the two previous planes. The scatter points show our magnetopause detection as well as the points in the magnetosphere and magnetosheath used to derive the Kelvin-Helmholtz instability growth rate.

APPENDIX B: Local simulation of the KH vortices at the magnetopause.

In a simplified slab geometry, we assume $\hat{x}$ to be perpendicular to the unperturbed magnetopause, $\hat{y}$ along the flow and $\hat{z}$ represents the latitude direction. We start from a slab MHD equilibrium, depending on x and z only, that mimics the gradual stabilization of the KH instability away from z = 0 where the growth rate is maximal. In this equilibrium, all physical quantities but the x and z-component of the magnetic field are functions of the flow-aligned component Ψ of the equilibrium vector potential [*Andreussi et al*., 2012] while $B_{x,eq}$ and $B_{z,eq}$ are simply given by the rotational of $\psi\hat{y}$.

We set $\psi(x,z) = B_{z,av}[4/3x + L_z/3\pi\,\sinh(2\pi x/L_z)\cos(2\pi z/L_z)]/2$ and $B_{y,eq} = B_{flow}(1 + \tanh(\Psi/a))$, where a is the half-width of the unperturbed magnetopause, $B_{z,av}$ the averaged northward field and B_{flow} the flow-aligned component of the IMF (all quantities are normalized to the ion skip depth d_i, the ion cyclotron frequency Ω_{ci} and the ion mass m_i. Taking $x \in [-L_x/2, +L_x/2]$ and $a \ll L_x \ll L_z$ we obtain a magnetic field that is nearly northward inside the magnetosphere and that has a flow aligned component B_{flow} outside it.

The high-latitude stabilization is achieved assuming $U_{eq} = \Delta U/2\,\tanh(\psi/a)\hat{y}$. Indeed the velocity gradient at the magnetopause (x = 0) is three times bigger at z = 0 than its value at the z-boundaries at $z = \pm L_z/2$. Consequently, the KH instability grows much faster around z = 0 than at high latitudes [*Faganello et al*., 2012a] that remain nearly unperturbed during the development of the instability at low latitude.

The plasma density is given by $n_{eq} = n_{av} + |n_{sh} - n_{sp}|/2\,\tanh(\psi/a)$, where , n_{sh}, n_{sp}, and n_{av} are the magnetosheath, the magnetosphere and the average density, respectively. The thermal pressure assures $P_{th,eq} + B_{flow}^2/2 = \Pi = cst$, so that the Grad-Shafranov equation (force-balance equation in field-aligned coordinates) $\nabla^2\psi = \partial_\psi \Pi$ is satisfied. We set the ratio between the ion and electron temperatures equal to four. All the plasma quantities are taken as close as possible to those measured by MMS satellites across the magnetopause and are resumed in Table 1.

The system evolution is described by Hall-MHD equations that include the electron diamagnetic term and a small but finite resistivity ($\eta = 10^{-3}$ in adimensional units) in the generalized Ohm's law. We consider adiabatic closures for both ions and electrons. All equations are advanced in time by a 4th-order Runge-Kutta scheme. Spatial derivatives are performed via 6th-order finite differences along the periodic y and z directions, while using a 4th-order compact implicit scheme [*Lele*, 1992] for the more critical open x-direction. At the x-boundaries, we adopt a decomposition on MHD characteristic that lets all MHD perturbations simply leave the domain [*Landi et al*., 2005; *Faganello et al*., 2009].

We set the magnetopause half-width a = 3, consequently the wavelength (along $\hat{y}$) of the more instable KH mode is $\lambda_{KH} \approx 12\pi$. Taking an "effective" ion skin depth $d_i \approx 300\ km$ we obtain a physical wavelength $\approx 12000\ km$ (in practice the importance of the Hall term is slightly enhanced in our simulation but we are able to correctly resolve di).

The box dimensions are $L_x = 60$, $L_y = 24\pi$, and $L_z = 120\pi$, so that the KH instability develops two vortices along $\hat{y}$. The number of points in each direction is $n_x = 600$, $n_y = 512$, $nz = 512$. Lz was chosen from the outcome of the global simulation. It is compatible with the global simulations and allows for a sufficient instability, compared to KH vortex size, so as to allow vortex pairing in the non-linear stage. The unstable zone needs to be sufficiently thick, as shown in *Takagi et al.* [2006].

Finally, the density on the magnetospheric side is n = 6.5 cm^{-3}, and the plasma β = 1.82, while on the magnetosheath side these parameters are n = 19.5 cm^{-3} and β = 1.58, consistent with MMS observations.

Acknowledgments

Simulation results have been provided by the Community Coordinated Modeling Center at Goddard Space Flight Center through their public Runs on Request system (http://ccmc.gsfc.nasa.gov). The BATS-R-US Model was developed by Dr. Tamas Gombosi at the University of Michigan. The run is stored at: https://ccmc.gsfc.nasa.gov/results/viewrun.php?domain=GM&runnumber=Yoann_Vernisse_012518_1. The two-fluid simulation data are stored in the PIIM laboratory repository and are available at https://storagepiim.etoile.univ-amu.fr/share.cgi?ssid=00SbRzp. For MMS data visit https://lasp.colorado.edu/mms/sdc/public/. We thank all the MMS teams for their remarkable work and great hardware accomplishments. IRAP contribution to MMS was performed with the support of CNRS and CNES. FC has received funding from the European Union's Horizon 2020 research and innovation programme under grant agreement No 776262 (AIDA).

Bibliography

Andreussi, T., Morrison, P. J., & Pegoraro, F. (2012). Hamiltonian magnetohydrodynamics: Helically symmetric formulation, Casimir invariants, and equilibrium variational principles. *Physics of Plasmas*, *19*, 052102. https://doi.org/10.1063/1.4714761

Borgogno, D., Califano, F., Faganello, M., & Pegoraro, F. (2015). Double-reconnected magnetic structures driven by Kelvin-Helmholtz vortices at the Earth's magnetosphere. *Physics of Plasmas*, *22*(3), 032301. https://doi.org/10.1063/1.4913578

Burch, J. L., Moore, T. E., Torbert, R. B., & Giles, B. L. (2015). Magnetospheric Multiscale Overview and Science Objectives. *Space Science Reviews*. https://doi.org/10.1007/s11214-015-0164-9

Burch, J. L., Torbert, R. B., Phan, T. D., Chen, L.-J., Moore, T. E., Ergun, R. E., … Chandler, M. (2016). Electron-scale measurements of magnetic reconnection in space. *Science*. https://doi.org/10.1126/science.aaf2939

Chandrasekhar, S. (1961). *Hydrodynamic and hydromagnetic stability*. Consulté à l'adresse http://cdsads.u-strasbg.fr/abs/1961hhs..book.....C

Chen, Q., Otto, A., & Lee, L. C. (1997). Tearing instability, Kelvin-Helmholtz instability, and magnetic reconnection. *Journal of Geophysical Research*, *102*, 151-162. https://doi.org/10.1029/96JA03144

Eriksson, S., Lavraud, B., Wilder, F. D., Stawarz, J. E., Giles, B. L., Burch, J. L., … Goodrich, K. A. (2016). Magnetospheric Multiscale observations of magnetic reconnection associated with Kelvin-Helmholtz waves. *Geophysical Research Letters*, *43*, 5606-5615. https://doi.org/10.1002/2016GL068783

Fadanelli, S., Faganello, M., Califano, F., Cerri, S. S., Pegoraro, F., & Lavraud, B. (2018). North-South asymmetric Kelvin-Helmholtz instability and induced reconnection at the Earth's magnetospheric flanks. *ArXiv e-prints*, *1805*, arXiv:1805.01466.

Faganello, M., Califano, F., & Pegoraro, F. (2008). Time Window for Magnetic Reconnection in Plasma Configurations with Velocity Shear. *Physical Review Letters*, *101*, 175003. https://doi.org/10.1103/PhysRevLett.101.175003

Faganello, M., Califano, F., & Pegoraro, F. (2009). Being on time in magnetic reconnection. *New Journal of Physics*, *11*, 063008. https://doi.org/10.1088/1367-2630/11/6/063008

Faganello, M., Califano, F., Pegoraro, F., & Andreussi, T. (2012a). Double mid-latitude dynamical reconnection at the magnetopause: An efficient mechanism allowing solar wind to enter the Earth's magnetosphere. *EPL (Europhysics Letters)*, *100*, 69001. https://doi.org/10.1209/0295-5075/100/69001

Faganello, M., Califano, F., Pegoraro, F., Andreussi, T., & Benkadda, S. (2012b). Magnetic reconnection and Kelvin-Helmholtz instabilities at the Earth's magnetopause. *Plasma Physics and Controlled Fusion*, *54*(12), 124037. https://doi.org/10.1088/0741-3335/54/12/124037

Faganello, M., Califano, F., Pegoraro, F., & Retinò, A. (2014). Kelvin-Helmholtz vortices and double mid-latitude reconnection at the Earth's magnetopause: Comparison between observations and simulations. *EPL (Europhysics Letters)*, *107*, 19001. https://doi.org/10.1209/0295-5075/107/19001

Faganello, Matteo, & Califano, F. (2017). Magnetized Kelvin-Helmholtz instability: theory and simulations in the Earth's magnetosphere context. *Journal of Plasma Physics*, *83*, 535830601. https://doi.org/10.1017/S0022377817000770

Fairfield, D. H., Otto, A., Mukai, T., Kokubun, S., Lepping, R. P., Steinberg, J. T., … Yamamoto, T. (2000). Geotail observations of the Kelvin-Helmholtz instability at the equatorial magnetotail boundary for parallel northward fields. *Journal of Geophysical Research*, *105*, 21. https://doi.org/10.1029/1999JA000316

Farrugia, C. J., Gratton, F. T., Bender, L., Biernat, H. K., Erkaev, N. V., Quinn, J. M., … Dennisenko, V. (1998). Charts of joint Kelvin-Helmholtz and Rayleigh-Taylor instabilites at the dayside magnetopause for strongly northward interplanetary magnetic field. *Journal of Geophysical Research*, *103*, 6703-6728. https://doi.org/10.1029/97JA03248

Foullon, C., Farrugia, C. J., Owen, C. J., Fazakerley, A. N., & Gratton, F. T. (2010). Kelvin-Helmholtz Multi-Spacecraft Studies at the Earth's Magnetopause Boundaries. *Twelfth International Solar Wind Conference*, *1216*, 483-486. https://doi.org/10.1063/1.3395908

Frank, A., Jones, T. W., Ryu, D., & Gaalaas, J. B. (1996). The Magnetohydrodynamic Kelvin-Helmholtz Instability: A Two-dimensional Numerical Study. *The Astrophysical Journal*, *460*, 777. https://doi.org/10.1086/177009

Fuselier, S. A., Anderson, B. J., & Onsager, T. G. (1995). Particle signatures of magnetic topology at the magnetopause: AMPTE/CCE observations. *Journal of Geophysical Research*, *100*, 11. https://doi.org/10.1029/94JA02811

Fuselier, S. A., Anderson, B. J., & Onsager, T. G. (1997). Electron and ion signatures of field line topology at the low-shear magnetopause. *Journal of Geophysical Research*, *102*, 4847-4864. https://doi.org/10.1029/96JA03635

Fuselier, S. A., Vines, S. K., Burch, J. L., Petrinec, S. M., Trattner, K. J., Cassak, P. A., … Webster, J. M. (2017). Large-scale characteristics of reconnection diffusion regions and associated magnetopause crossings observed by MMS. *Journal of Geophysical Research (Space Physics)*, *122*, 5466-5486. https://doi.org/10.1002/2017JA024024

Gosling, J. T., & Phan, T. D. (2013). Magnetic Reconnection in the Solar Wind at Current Sheets Associated with Extremely Small Field Shear Angles. *The Astrophysical Journal Letters*, *763*, L39. https://doi.org/10.1088/2041-8205/763/2/L39

Harvey, C. C. (1998). Spatial Gradients and the Volumetric Tensor. *ISSI Scientific Reports Series*, *1*, 307-322.

Hasegawa, H., Fujimoto, M., Phan, T.-D., Rème, H., Balogh, A., Dunlop, M. W., … TanDokoro, R. (2004). Transport of solar wind into Earth's magnetosphere through rolled-up Kelvin-Helmholtz vortices. *Nature*, *430*, 755-758. https://doi.org/10.1038/nature02799

Hesse, M., Aunai, N., Birn, J., Cassak, P., Denton, R. E., Drake, J. F., … Zenitani, S. (2016). Theory and Modeling for the Magnetospheric Multiscale Mission. *Space Science Reviews*, *199*, 577-630. https://doi.org/10.1007/s11214-014-0078-y

Kavosi, S., & Raeder, J. (2015). Ubiquity of Kelvin-Helmholtz waves at Earth's magnetopause. *Nature Communications*, *6*, 7019. https://doi.org/10.1038/ncomms8019

King, J. H., & Papitashvili, N. E. (2005). Solar wind spatial scales in and comparisons of hourly Wind and ACE plasma and magnetic field data. *Journal of Geophysical Research: Space Physics*, *110*(A2), n/a–n/a. https://doi.org/10.1029/2004JA010649

Knoll, D. A., & Chacón, L. (2002). Magnetic Reconnection in the Two-Dimensional Kelvin-Helmholtz Instability. *Physical Review Letters*, *88*, 215003. https://doi.org/10.1103/PhysRevLett.88.215003

Kobayashi, S., Rogers, B. N., & Numata, R. (2014). Gyrokinetic simulations of collisionless reconnection in turbulent non-uniform plasmas. *Physics of Plasmas*, *21*, 040704. https://doi.org/10.1063/1.4873703

Landi, S., Velli, M., & Einaudi, G. (2005). Alfvén Waves and Shock Wave Formation at an X-Point Magnetic Field Configuration. *The Astrophysical Journal*, *624*, 392-401. https://doi.org/10.1086/428822

Lavraud, B., Thomsen, M. F., Lefebvre, B., Schwartz, S. J., Seki, K., Phan, T. D., … Balogh, A. (2006). Evidence for newly closed magnetosheath field lines at the dayside magnetopause under northward IMF. *Journal of Geophysical Research (Space Physics)*, *111*, A05211. https://doi.org/10.1029/2005JA011266

Lavraud, B., Thomsen, M. F., Taylor, M. G. G. T., Wang, Y. L., Phan, T. D., Schwartz, S. J., … Balogh, A. (2005). Characteristics of the magnetosheath electron boundary layer under northward interplanetary magnetic field: Implications for high-latitude reconnection. *Journal of Geophysical Research (Space Physics)*, *110*, A06209. https://doi.org/10.1029/2004JA010808

Lele, S. K. (1992). Compact Finite Difference Schemes with Spectral-like Resolution. *Journal of Computational Physics*, *103*, 16-42. https://doi.org/10.1016/0021-9991(92)90324-R

Li, W., André, M., Khotyaintsev, Y. V., Vaivads, A., Graham, D. B., Toledo-Redondo, S., … Strangeway, R. J. (2016). Kinetic evidence of magnetic reconnection due to Kelvin-Helmholtz waves. *Geophysical Research Letters*, n/a–n/a. https://doi.org/10.1002/2016GL069192

Lin, D., Wang, C., Li, W., Tang, B., Guo, X., & Peng, Z. (2014). Properties of Kelvin-Helmholtz waves at the magnetopause under northward interplanetary magnetic field: Statistical study. *Journal of Geophysical Research (Space Physics)*, *119*, 7485-7494. https://doi.org/10.1002/2014JA020379

Liu, Y.-H., & Hesse, M. (2016). Suppression of collisionless magnetic reconnection in asymmetric current sheets. *Physics of Plasmas*, *23*, 060704. https://doi.org/10.1063/1.4954818

Liu, Z. X., & Hu, Y. D. (1988). Local magnetic reconnection caused by vortices in the flow field. *Geophysical Research Letters*, *15*, 752-755. https://doi.org/10.1029/GL015i008p00752

Ma, X., Delamere, P., Otto, A., & Burkholder, B. (2017). Plasma Transport Driven by the Three-Dimensional Kelvin-Helmholtz Instability. *Journal of Geophysical Research: Space Physics*, *122*(10), 2017JA024394. https://doi.org/10.1002/2017JA024394

Masters, A. (2014). Magnetic reconnection at Uranus' magnetopause. *Journal of Geophysical Research (Space Physics)*, *119*, 5520-5538. https://doi.org/10.1002/2014JA020077

Masters, A. (2015). Magnetic reconnection at Neptune's magnetopause. *Journal of Geophysical Research (Space Physics)*, *120*, 479-493. https://doi.org/10.1002/2014JA020744

Masters, A., Eastwood, J. P., Swisdak, M., Thomsen, M. F., Russell, C. T., Sergis, N., … Krimigis, S. M. (2012). The importance of plasma β conditions for magnetic reconnection at Saturn's magnetopause. *Geophysical Research Letters*, *39*, L08103. https://doi.org/10.1029/2012GL051372

McNally, C. P., Lyra, W., & Passy, J.-C. (2012). A Well-posed Kelvin-Helmholtz Instability Test and Comparison. *The Astrophysical Journal Supplement Series*, *201*, 18. https://doi.org/10.1088/0067-0049/201/2/18

Miura, A., & Pritchett, P. L. (1982). Nonlocal stability analysis of the MHD Kelvin-Helmholtz instability in a compressible plasma. *Journal of Geophysical Research*, *87*, 7431-7444. https://doi.org/10.1029/JA087iA09p07431

Miura, Akira. (1995). Dependence of the magnetopause Kelvin-Helmholtz instability on the orientation of the magnetosheath magnetic field. *Geophysical Research Letters*, *22*, 2993-2996. https://doi.org/10.1029/95GL02793

Nakamura, T. K. M., & Fujimoto, M. (2005). Magnetic reconnection within rolled-up MHD-scale Kelvin-Helmholtz vortices: Two-fluid simulations including finite electron inertial effects. *Geophysical Research Letters*, *32*, L21102. https://doi.org/10.1029/2005GL023362

Nakamura, T. K. M., Fujimoto, M., & Otto, A. (2008). Structure of an MHD-scale Kelvin-Helmholtz vortex: Two-dimensional two-fluid simulations including finite electron inertial effects. *Journal of Geophysical Research (Space Physics)*, *113*, A09204. https://doi.org/10.1029/2007JA012803

Nakamura, T. K. M., Hasegawa, H., Shinohara, I., & Fujimoto, M. (2011). Evolution of an MHD-scale Kelvin-Helmholtz vortex accompanied by magnetic reconnection: Two-dimensional particle simulations. *Journal of Geophysical Research (Space Physics)*, *116*, A03227. https://doi.org/10.1029/2010JA016046

Nakamura, T. K. M., Daughton, W., Karimabadi, H., & Eriksson, S. (2013). Three-dimensional dynamics of vortex-induced reconnection and comparison with THEMIS observations. Journal of Geophysical Research: Space Physics, 118, 5742– 5757. https://doi.org/10.1002/jgra.50547

Nakamura, T. K. M., Eriksson, S., Hasegawa, H., Zenitani, S., Li, W. Y., Genestreti, K. J., … Daughton, W. (2017a), Mass and energy transfer across the Earth's magnetopause caused by

vortex-induced reconnection. *Journal of Geophysical Research: Space Physics*, 2017JA024346. https://doi.org/10.1002/2017JA024346

Nakamura, T. K. M., Hasegawa, H., Daughton, W., Eriksson, S., Li, W. Y., & Nakamura, R. (2017b). Turbulent mass transfer caused by vortex induced reconnection in collisionless magnetospheric plasmas. *Nature Communications*, *8*, 1582. https://doi.org/10.1038/s41467-017-01579-0

Nykyri, K., Otto, A., Lavraud, B., Mouikis, C., Kistler, L. M., Balogh, A., & Rème, H. (2006). Cluster observations of reconnection due to the Kelvin-Helmholtz instability at the dawnside magnetospheric flank. *Annales Geophysicae*, *24*, 2619-2643. https://doi.org/10.5194/angeo-24-2619-2006

Nykyri, Katariina, Ma, X., Dimmock, A., Foullon, C., Otto, A., & Osmane, A. (2017). Influence of velocity fluctuations on the Kelvin-Helmholtz instability and its associated mass transport. *Journal of Geophysical Research (Space Physics)*, *122*, 9489-9512. https://doi.org/10.1002/2017JA024374

Onsager, T. G., Scudder, J. D., Lockwood, M., & Russell, C. T. (2001). Reconnection at the high-latitude magnetopause during northward interplanetary magnetic field conditions. *Journal of Geophysical Research*, *106*, 25467-25488. https://doi.org/10.1029/2000JA000444

Otto, A., & Fairfield, D. H. (2000). Kelvin-Helmholtz instability at the magnetotail boundary: MHD simulation and comparison with Geotail observations. *Journal of Geophysical Research*, *105*, 21. https://doi.org/10.1029/1999JA000312

Phan, T. D., Gosling, J. T., Paschmann, G., Pasma, C., Drake, J. F., Øieroset, M., … Davis, M. S. (2010). The Dependence of Magnetic Reconnection on Plasma β and Magnetic Shear: Evidence from Solar Wind Observations. *The Astrophysical Journal Letters*, *719*, L199-L203. https://doi.org/10.1088/2041-8205/719/2/L199

Phan, T. D., Love, T. E., Gosling, J. T., Paschmann, G., Eastwood, J. P., Oieroset, M., … Auster, U. (2011). Triggering of magnetic reconnection in a magnetosheath current sheet due to compression against the magnetopause. *Geophysical Research Letters, 38*, L17101. https://doi.org/10.1029/2011GL048586

Phan, T. D., Paschmann, G., Gosling, J. T., Oieroset, M., Fujimoto, M., Drake, J. F., & Angelopoulos, V. (2013). The dependence of magnetic reconnection on plasma β and magnetic shear: Evidence from magnetopause observations. *Geophysical Research Letters, 40*, 11-16. https://doi.org/10.1029/2012GL054528

Phan, T., Dunlop, M., Paschmann, G., Klecker, B., Bosqued, J., Rème, H., … Kistler, L. (2004a). Cluster observations of continuous reconnection at the magnetopause under steady interplanetary magnetic field conditions. *Annales Geophysicae, 22*, 2355-2367. https://doi.org/10.5194/angeo-22-2355-2004

Phan, T., Dunlop, M., Paschmann, G., Klecker, B., Bosqued, J., Rème, H., … Kistler, L. (2004b). Cluster observations of continuous reconnection at the magnetopause under steady interplanetary magnetic field conditions. *Annales Geophysicae, 22*, 2355-2367. https://doi.org/10.5194/angeo-22-2355-2004

Powell, K. G., Roe, P. L., Linde, T. J., Gombosi, T. I., & De Zeeuw, D. L. (1999). A Solution-Adaptive Upwind Scheme for Ideal Magnetohydrodynamics. *Journal of Computational Physics, 154*, 284-309. https://doi.org/10.1006/jcph.1999.6299

Priest, E., & Forbes, T. (2000). Unsteady Reconnection: The Tearing Mode. In *Magnetic reconnection : MHD theory and applications* (p. 177-204). Cambridge University Press.

812 Raeder, J., Larson, D., Li, W., Kepko, E. L., & Fuller-Rowell, T. (2008). OpenGGCM Simulations for
813 the THEMIS Mission. *Space Science Reviews, 141*, 535-555. https://doi.org/10.1007/s11214-
814 008-9421-5
815 Shue, J.-H., Chao, J. K., Fu, H. C., Russell, C. T., Song, P., Khurana, K. K., & Singer, H. J. (1997). A
816 new functional form to study the solar wind control of the magnetopause size and shape. *Journal*
817 *of Geophysical Research, 102*, 9497-9512. https://doi.org/10.1029/97JA00196
818 Sonnerup, B. U. Ö., & Scheible, M. (1998). Minimum and Maximum Variance Analysis. *ISSI*
819 *Scientific Reports Series, 1*, 185-220.
820 Stawarz, J. E., Eriksson, S., Wilder, F. D., Ergun, R. E., Schwartz, S. J., Pouquet, A., … Sturner, A. P.
821 (2016). Observations of turbulence in a Kelvin-Helmholtz event on 8 September 2015 by the
822 Magnetospheric Multiscale mission. *Journal of Geophysical Research (Space Physics), 121*, 11.
823 https://doi.org/10.1002/2016JA023458
824 Swisdak, M., Opher, M., Drake, J. F., & Alouani Bibi, F. (2010). The Vector Direction of the
825 Interstellar Magnetic Field Outside the Heliosphere. *The Astrophysical Journal, 710*, 1769-1775.
826 https://doi.org/10.1088/0004-637X/710/2/1769
827 Swisdak, M., Rogers, B. N., Drake, J. F., & Shay, M. A. (2003). Diamagnetic suppression of
828 component magnetic reconnection at the magnetopause. *Journal of Geophysical Research (Space*
829 *Physics), 108*, 1218. https://doi.org/10.1029/2002JA009726
830 Takagi, K., Hashimoto, C., Hasegawa, H., Fujimoto, M., and TanDokoro, R. (2006), Kelvin-
831 Helmholtz instability in a magnetotail flank-like geometry: Three-dimensional MHD simulations,
832 J. Geophys. Res., 111, A08202, doi:10.1029/2006JA011631.
833 Vernisse, Y., Lavraud, B., Eriksson, S., Gershman, D. J., Dorelli, J., Pollock, C., … Yokota, S. (2016).
834 Signatures of complex magnetic topologies from multiple reconnection sites induced by Kelvin-

Helmholtz instability. *Journal of Geophysical Research: Space Physics*, *121*(10), 9926–9939. https://doi.org/10.1002/2016JA023051

Wilber, M., & Winglee, R. M. (1995). Dawn-dusk asymmetries in the low-latitude boundary layer arising from the Kelvin-Helmholtz instability: A particle simulation. *Journal of Geophysical Research*, *100*, 1883-1898. https://doi.org/10.1029/94JA02488

	$B_{z,av}$	B_{flow}	ΔU	n_{av}	Δn	T_{av}	ΔT
Normalized	1	-0.3	0.9	1	1	15/16	~ -1.3
physical	67 nT	-20 nT	360 km/s	13 cm^{-3}	13 cm^{-3}	1500 eV	2080 eV

Table 1: Equilibrium quantities expressed in normalized and physical units. We recall that the subscript "av" denotes the averaged values that these quantities have at the magnetopause.

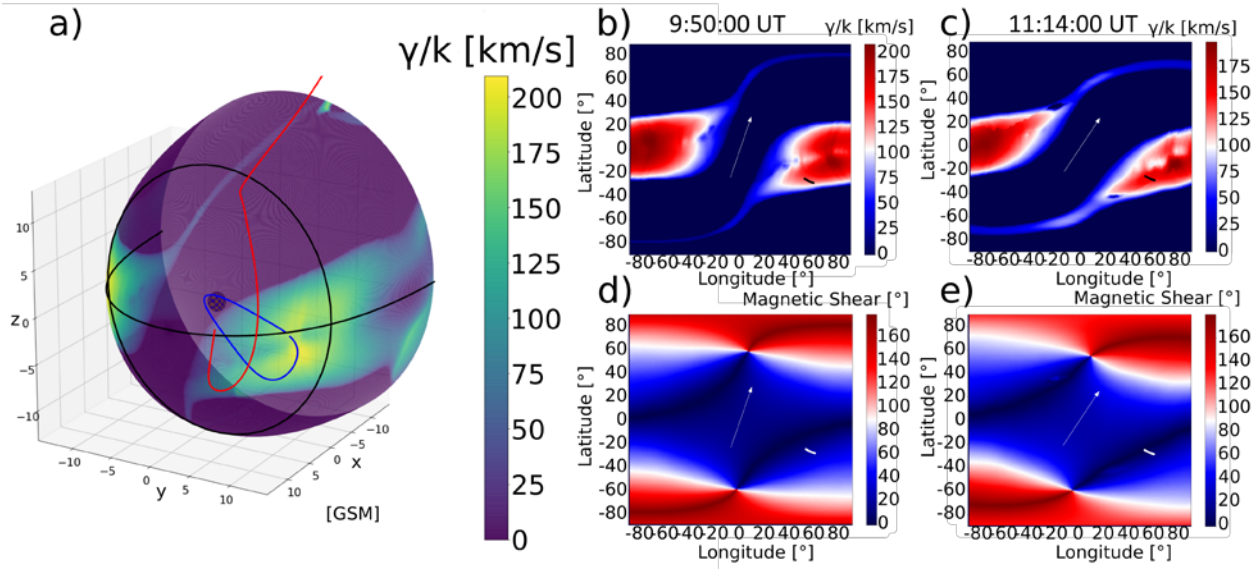

Figure 1:

Results from the three-dimensional MHD simulation code Bats'R'us in the GSM coordinate system. Inputs of the simulation are provided by the OMNI data. Panel a: three-dimensional representation of the growth rate calculated at the magnetopause. The terminator (black), the equatorial plane (black), the

orbit of the MMS spacecraft (blue), and a magnetic field line (red) are plotted(see text for detail). Panels b and c represent the growth rate at the magnetopause at 9:50:00 UT and 11:14:00 UT, respectively, while Panels d and e present the magnetic shear angle at the magnetopause at the same time. The IMF clock angle is represented by a white arrow in panels b to e. The positions of the MMS spacecraft from 8:30 UT to 11:30 UT are represented by black dots in panels b and c, and white dots in panels d and e.

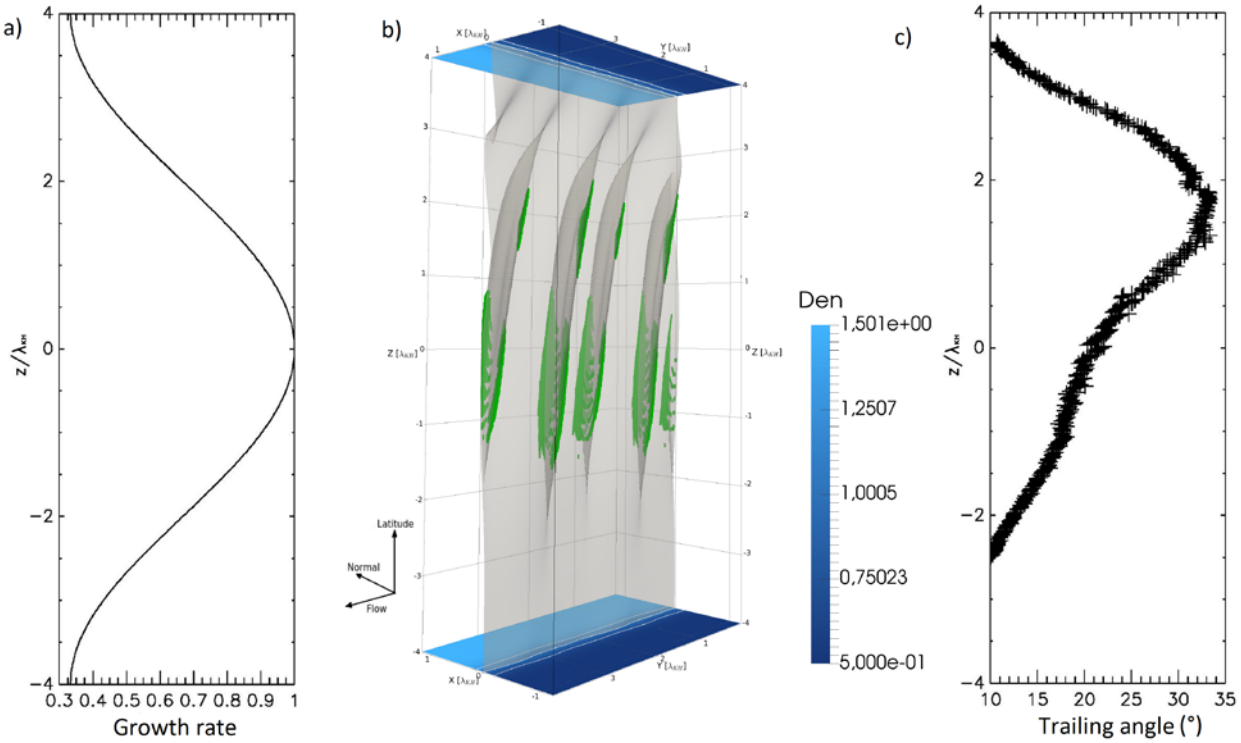

Figure 2:

Results from the local two-fluid simulation. a) normalized KH growth rate as a function of z. b) a 3D rendering of the simulation results at the beginning of the non-linear phase ($t\omega_{ci} = 525$). Blue and light blue colors represent the plasma density. White lines in the upper and lower planes are drawn at normalized plasma density = 0.7, 1.0, 1.3. The shaded surface represents the magnetopause folded by the vortices. Regions where the component of the magnetic field perpendicular to the folded magnetopause has a magnitude larger than 2% of the magnetospheric field are drawn in green. c) the trailing angle as a function of z at $t\omega_{ci} = 525$.

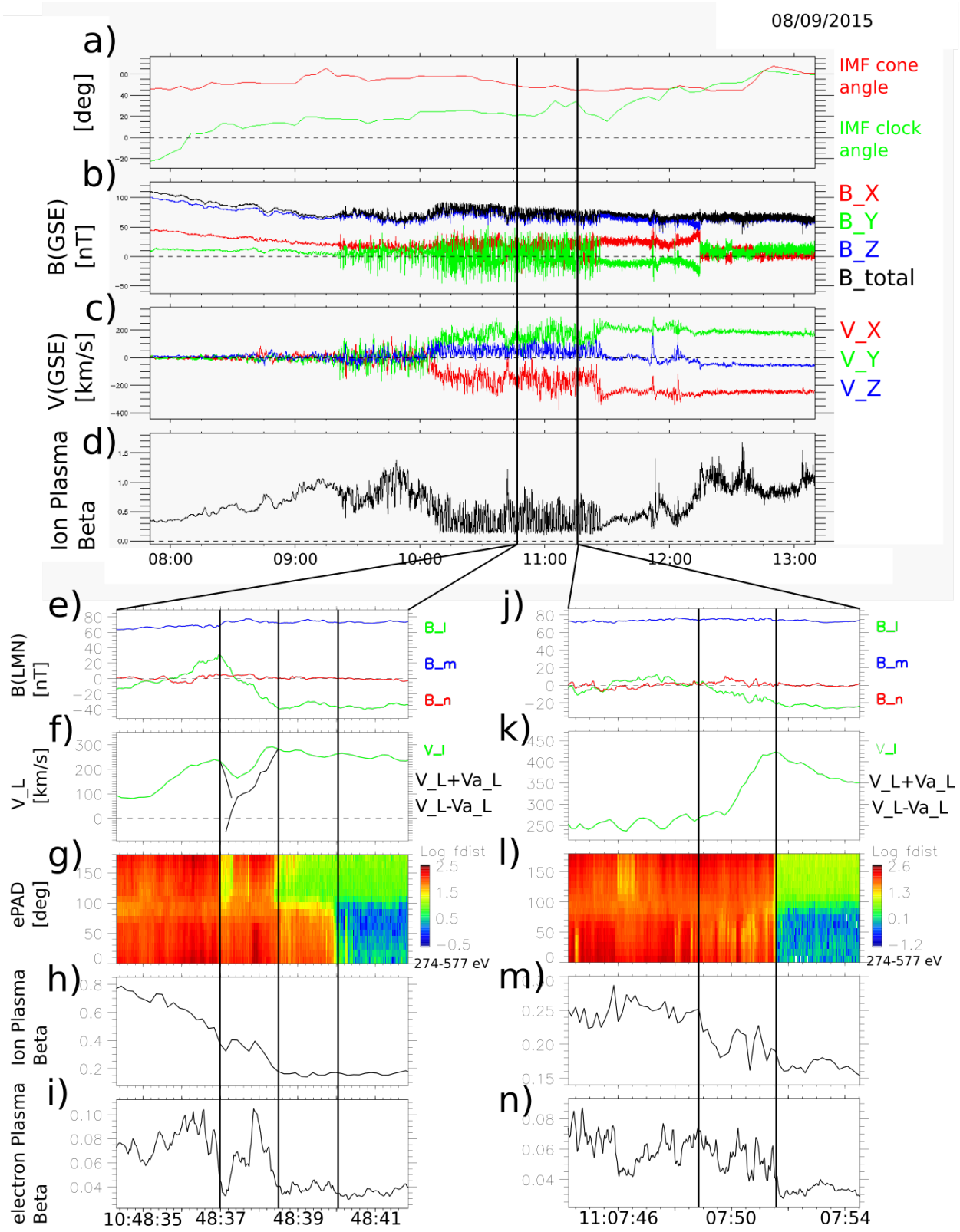
08/09/2015
a)
[deg]
IMF cone angle
IMF clock angle
b)
B(GSE) [nT]
B_X
B_Y
B_Z
B_total
c)
V(GSE) [km/s]
V_X
V_Y
V_Z
d)
Ion Plasma Beta
08:00
09:00
10:00
11:00
12:00
13:00
e)
B(LMN) [nT]
B_l
B_m
B_n
f)
V_L [km/s]
V_l
V_L+Va_L
V_L-Va_L
g)
ePAD [deg]
Log fdist
274-577 eV
h)
Ion Plasma Beta
i)
electron Plasma Beta
10:48:35
48:37
48:39
48:41
j)
B_l
B_m
B_n
k)
V_l
V_L+Va_L
V_L-Va_L
l)
Log fdist
274-577 eV
m)
n)
11:07:46
07:50
07:54

Figure 3:

Panel a): IMF cone angle and clock angle (in GSM) derived from OMNI data. Panels b), c), and d): Magnetic field, velocity, and ion plasma beta from the MMS1 spacecraft (GSE coordinate system). Data are from 08:00 to 13:00 UTC. Panels e) to j): current sheet crossing between 10:30:12 and 10:30:18. The magnetic field (panel e) is provided in the local LMN coordinate system. The Walén test is illustrated in panel f). Panel g) shows the electron pitch angle distribution for the energy 274-577eV. Panel i) show the ion plasma beta while panel j shows the electron plasma beta. The first two black lines delimit the current sheet and the second and third black lines delimit the electron boundary layer. Panels k) to o) are similar to Panels e) to j) with data between 11:07:45 and 11:07:54. The two solid black lines delimit the current sheet.

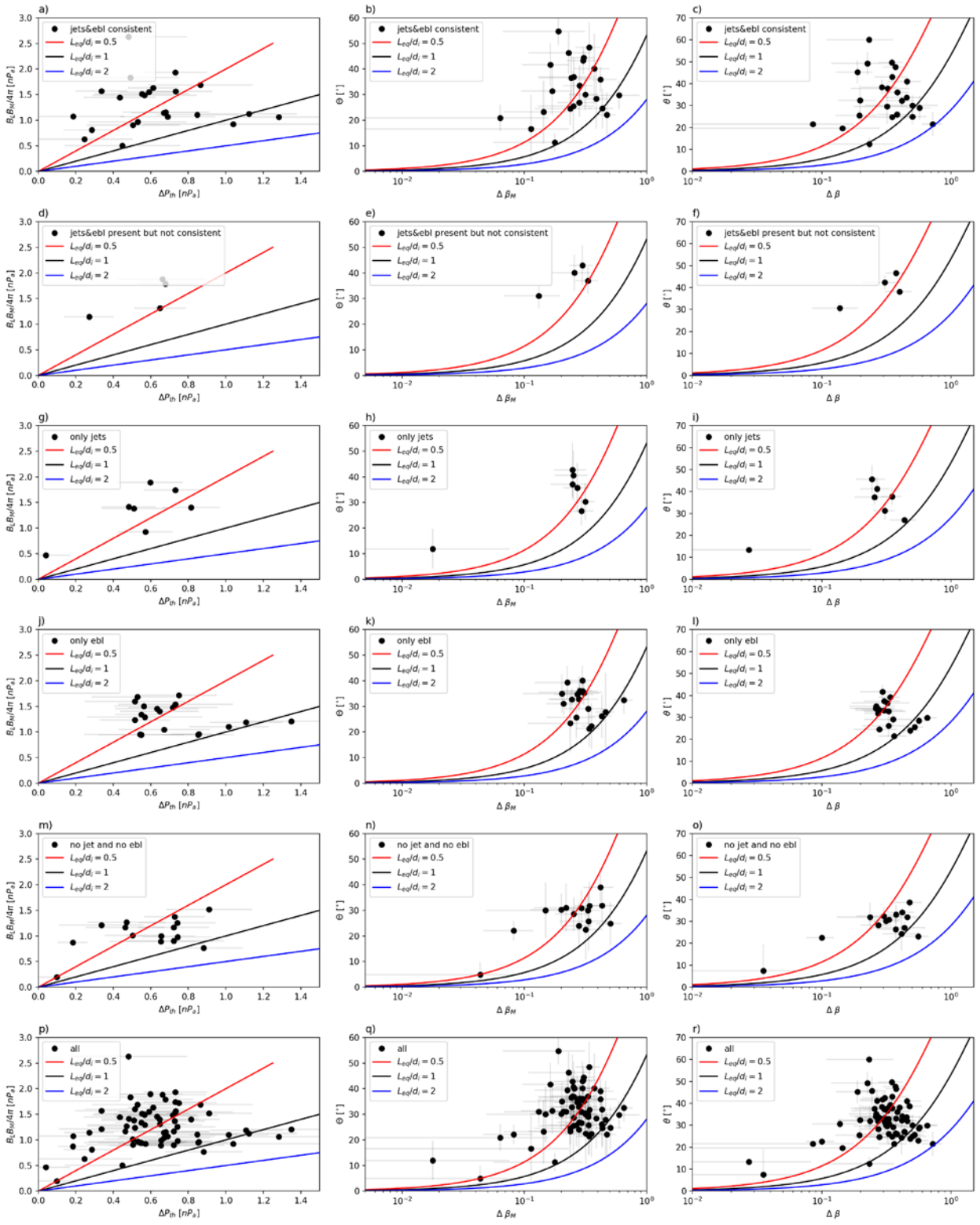

Figure 4:

Test of the *Swisdak et al.* [2003] model (see Equations 1, 2, and 3) for 69 current sheets crossings. The first, second and third column use Equations (1), (2), and (3), respectively. First row to second to last row

represent likelihood of events presenting magnetic reconnection signatures. The last row gathers all crossings at once. In each panel is represented the reconnection suppression condition for $L_{eq}/d_i = 0.5$, $1, and\ 2$ in red, black, and blue, respectively. Events which satisfy the model (i.e., where reconnection is allowed) are expected above the curves while suppressed events should be located under the curves.

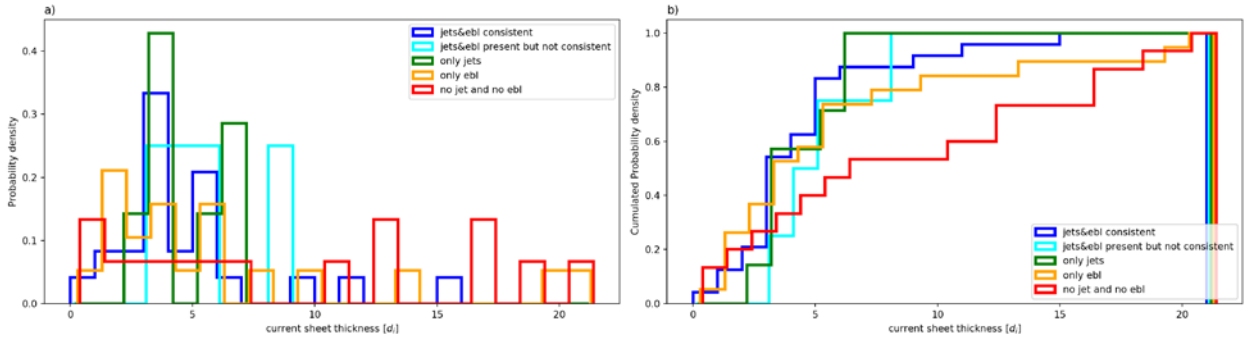

Figure 5:

Distributions of current sheet thicknesses (in inertial length) with their likelihood of being reconnecting events. Panel a) presents the normalize distributions of thicknesses, and Panel b) presents the cumulative distributions.

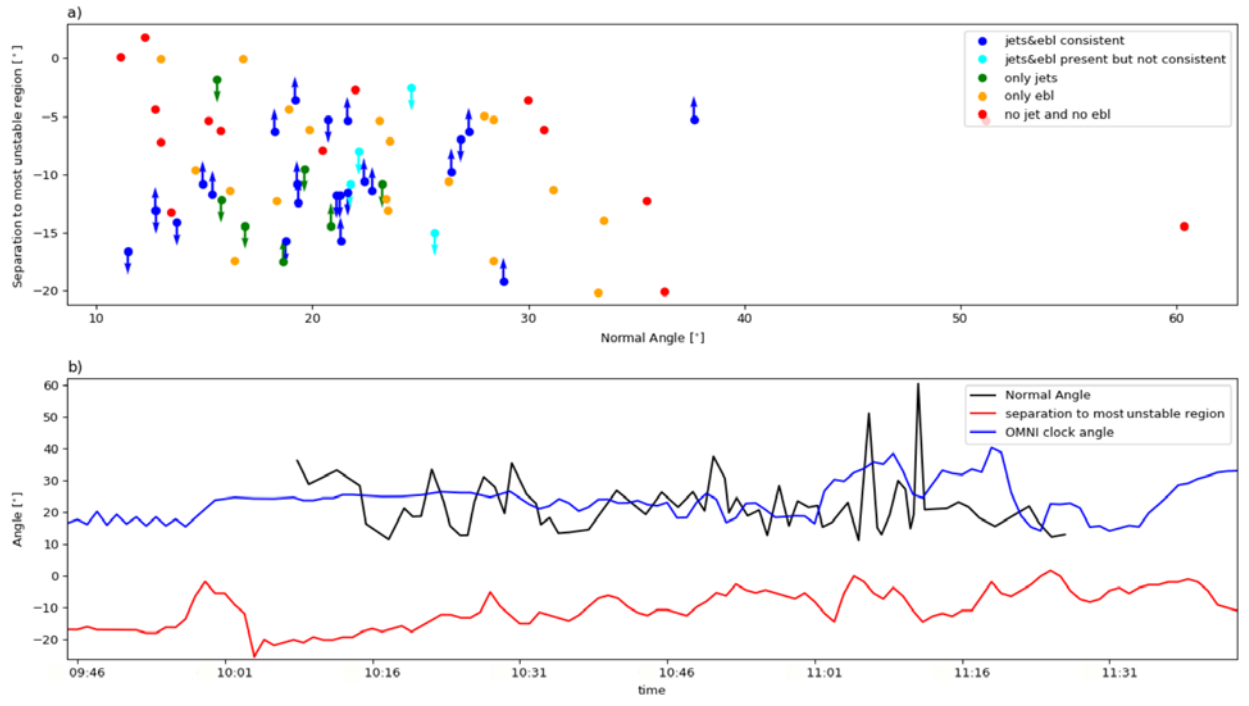

Figure 6:

Panel a: latitude distance (in degrees) between the MMS spacecraft and the most unstable plane derived from the global MHD model as a function of the angle between the normal of each current sheet and the normal of the unperturbed magnetopause ("normal angle"). The directionalities of the jets in accordance with the magnetic field geometry are represented with arrows. Events are grouped by their observed signatures. Panel b): time series during the observation of the KH instability at the magnetopause. The panel shows the "normal angle" in black, the OMNI clock angle in blue, and the separation between the spacecraft and the most unstable plane (in red).

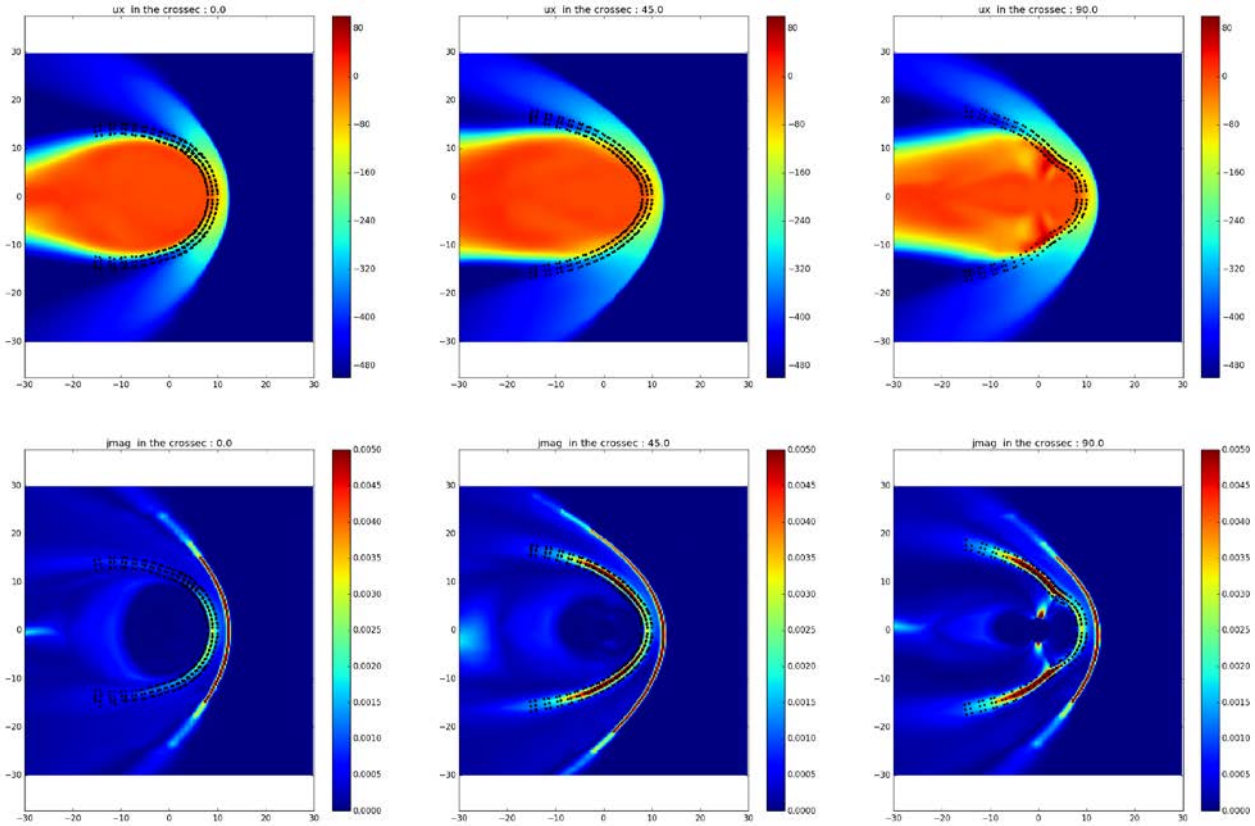

Figure 7

Results from CCMS's BATS'R'US simulation code. Bulk velocity and current density magnitude in two-dimensional cuts: equatorial plane, 45° plane, and meridional plane. The scatter points represent the magnetopause detection results with the corresponding magnetospheric and magnetosheath points.